Materials for Quantum Technology

PAPER • **OPEN ACCESS**

Low-loss α-tantalum coplanar waveguide resonators on silicon wafers: fabrication, characterization and surface modification

To cite this article: D P Lozano *et al* 2024 *Mater. Quantum. Technol.* **4** 025801

IOP Publishing Mater. Quantum Technol. 4 (2024) 025801 https://doi.org/10.1088/2633-4356/ad4b8c

Materials for Quantum Technology

OPEN ACCESS

RECEIVED
31 December 2023

REVISED
2 April 2024

ACCEPTED FOR PUBLICATION
14 May 2024

PUBLISHED
31 May 2024

PAPER

Low-loss α-tantalum coplanar waveguide resonators on silicon wafers: fabrication, characterization and surface modification

D P Lozano[1,*], M Mongillo[1], X Piao[1], S Couet[1], D Wan[1], Y Canvel[1], A M Vadiraj[1], Ts Ivanov[1], J Verjauw[1,2], R Acharya[1,3], J Van Damme[1,3], F A Mohiyaddin[1], J Jussot[1], P P Gowda[1], A Pacco[1], B Raes[4], J Van de Vondel[4], I P Radu[1], B Govoreanu[1], J Swerts[1], A Potočnik[1] and K De Greve[1,3]

[1] Imec, Kapeldreef 75, Leuven B-3001, Belgium
[2] Department of Materials Engineering (MTM), KU Leuven, Leuven B-3000, Belgium
[3] Department of Electrical Engineering (ESAT), KU Leuven, Leuven B-3000, Belgium
[4] Department of Physics and Astronomy, KU Leuven, Leuven B-3000, Belgium
[*] Author to whom any correspondence should be addressed.

E-mail: Daniel.PerezLozano@imec.be

Keywords: superconductors, resonators, quantum computing

Supplementary material for this article is available online

Abstract

The performance of state-of-the-art superconducting quantum devices is currently limited by microwave dielectric loss at different interfaces. α-tantalum is a superconductor that has proven effective in reducing dielectric loss and improving device performance due to its thin low-loss oxide. Here, we demonstrate the fabrication of high-quality factor α-tantalum coplanar-waveguide resonators directly on pristine 300 mm silicon wafers over a variety of metal deposition conditions and perform a comprehensive material and electrical characterization study. Additionally, we apply a surface treatment based on hydrofluoric acid that allows us to modify different resonators surfaces, leading to a reduction in two-level system loss in the devices by a factor of three. This loss reduction can be entirely attributed to the removal of surface oxides. Our study indicates that large scale manufacturing of low-loss superconducting circuits should indeed be feasible and suggests a viable avenue to materials-driven advancements in superconducting circuit performance.

1. Introduction

Increasing qubit coherence time is essential for enhancing the capabilities of noisy intermediate-scale quantum processors, and crucial for reducing the error-correction overhead in future fault-tolerant quantum computers [1, 2]. Historically, several approaches have been explored to increase their performance such as, participation ratio engineering [3]—typically resulting in bigger qubits- as well as optimal control [4, 5], shielding [6] and signal filtering [7]. In contrast, the number of advancements based on understanding microscopic origin of decoherence and energy loss—including the judicious increase of the materials toolbox—is rather limited [8, 9], with most published work focusing on only a few well documented materials such as Al [10–15], Nb [16–20], TiN [21, 22], NbN [23, 24], NbTiN [25–27], granular-Al [28, 29], Re [30] and In [31]. Only recently, the suite of materials for superconducting quantum technology was further expanded, markedly resulting in qubit relaxation times as high as 0.5 ms for 2D transmon qubits by using α-tantalum (α-Ta) [32, 33]. It has been suggested that the simpler native oxide structure of tantalum [34, 35] compared to native oxide structures of other materials such as niobium (Nb) [36] leads to lower microwave loss. However, these studies employed sapphire as substrate, which has lower dielectric loss [37–39] than the high-resistivity silicon (Si) substrates [40, 41] typically used in superconducting circuits, potentially positively affecting the obtained relaxation times. Moreover, the use of sapphire substrates is incompatible with fabrication processes and requirements needed to manufacture and integrate large numbers of qubits in 300 mm industry-scale facilities. While the deposition of α-Ta directly on thermally oxidized Si [42] substrates has been known since the 90s, it is widely recognized that the silicon oxide at the silicon–tantalum interface has a detrimental effect on the performance of superconducting qubits and

resonators. To circumvent the issue, α-Ta coplanar-waveguide resonators, which are short loop proxies for superconducting qubits, have been fabricated with the help of seed layers such as Nb [43, 44], tantalum nitride (TaN) [45], and titanium nitride (TiN) [46]. Nonetheless, this approach adds to the processing complexity during both the deposition and etching stages of the metallic layers. Furthermore, it introduces an additional interface that could potentially harbor additional two-level system (TLS) defects [47], thereby potentially compromising the performance of the superconducting device. Recently,

LC α-Ta resonators have been deposited on pristine Si at elevated temperature [48]. However, due to unspecified design parameters and a frequency range not typically used for superconducting qubits, these results are difficult to compare to the other works and make it hard to judge the relevance of high-temperature fabrication processes for high-coherence quantum computing applications.

In this study, we demonstrate the fabrication of high-Q factor α-Ta coplanar-waveguide resonators on pristine 300 mm Si substrates over a wide temperature processing window that allows the growth of α-Ta films with different crystallographic texture and resistivity values. We characterize the microwave performance of the devices and show that our results are consistent with TLS-induced dissipation. We further implement and perform in-depth characterization of the metal-air (M-A), metal-substrate (M-S), and substrate-air (S-A) interfaces by combining spectroscopy and microscopy techniques to locate loss sources. Finally, by applying a surface treatment based on hydrofluoric acid (HF) we mitigate the TLS loss by a factor of three, reaching internal Q-factors as high as $4.5{\cdot}10^6$ at single photon powers and demonstrate that this loss reduction is associated to surface oxide removal.

2. Characterization of α-tantalum films

We sputter α-Ta films on HF-cleaned Si substrates at 400 °C, 450 °C and 500 °C [49] with a nominal thickness of 100 nm. To verify the growth of the correct phase, we measure the x-ray-diffraction (XRD) spectrum of each film. Two diffraction peaks (figure 1(a)) corresponding to α-Ta are visible, indicating the polycrystalline nature of our films, while peaks corresponding to β-Ta are not present. We also observe that the height of the (200) peak increases as a function of deposition temperature, indicating that each of the films have a different crystallographic texture. To further confirm the growth of the α-Ta phase, we also perform electrical characterization of the films by measuring electrical resistivity across the 300 mm wafers (figures 2(a)–(c)). Room temperature resistivity is a good probe to test the tantalum phase formation since β-Ta exhibits resistivity values around 150 $\mu\Omega$ cm–200 $\mu\Omega$ cm which is ten times higher than resistivity of the α-Ta phase 15 $\mu\Omega$ cm–20 $\mu\Omega$ cm [50]. Room-temperature resistivity of the three films is comparable to the typical resistivity of α-Ta films with similar thicknesses [51] and it only slightly increases as a function of deposition temperature. Furthermore, low variability of the resistivity across each wafer of less than 3% indicates the formation of purely the α-Ta phase without the presence of minority β-Ta phase patches [52]. The observed increase in resistivity across the various α-Ta films can be attributed to a increment in grain boundary density, resulting from both the reduction in grain size as the deposition temperature increases, shown by the increase in the full width at half maximum of the (110) peak, and the concurrent increase in number grains along the (200) orientation [53]. In order to electrically validate and investigate the respective deposition conditions and to study microwave loss sources and potential microwave loss differences between the three film types, we pattern coplanar-waveguide resonators using the 400 °C, 450 °C and 500 °C α-Ta films. Resonator fabrication is performed in a 300 mm fabrication facility using industry-standard fabrication processes involving subtractive (dry) etching similar to previous reports [54].

3. Resonator microwave characterization

We characterize the performance of the superconducting quarter-wave coplanar waveguide resonators by performing S_{21} transmission spectrum measurements at 10 mK. All eight resonators on a chip are fed by a common transmission line and have a 4.5 μm wide gap and 10 μm wide central trace, while their frequencies are distributed between 4 and 8 GHz by appropriately adjusting their length. A fitting routine [55] is used to extract the resonant frequency, f_r, internal quality factor Q_i, and coupling quality factor Q_c as a function of the estimated mean photon number in the different resonators investigated.

The resonators labeled as 'reference' correspond to as fabricated resonators without any post-processing, and the ones labeled as 'HF-treated' correspond to resonators that received a post-processing HF clean step not longer than 12 h before the packaging and cooling down in the dilution refrigerator. Apart from sample mounting and wire bonding, HF-treated resonators were stored in a N_2 atmosphere during the 12 h waiting period. The HF post-processing treatment is employed in an attempt to reduce surface oxides, which are the major source of loss in superconducting quantum devices [56]. We used the same treatment as previously

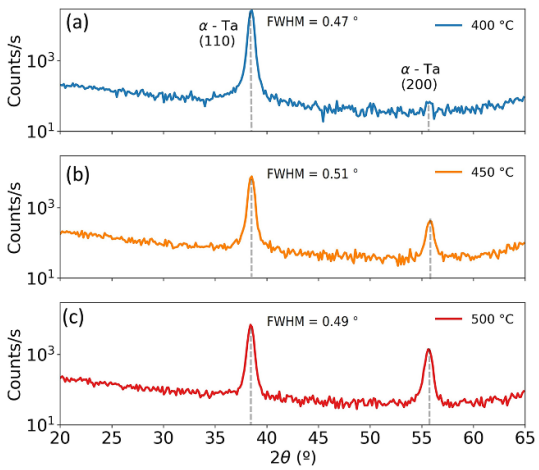

Figure 1. XRD spectra of the 400 °C (a), 450 °C (b) and 500 °C (c) α-Ta films used for resonator fabrication.

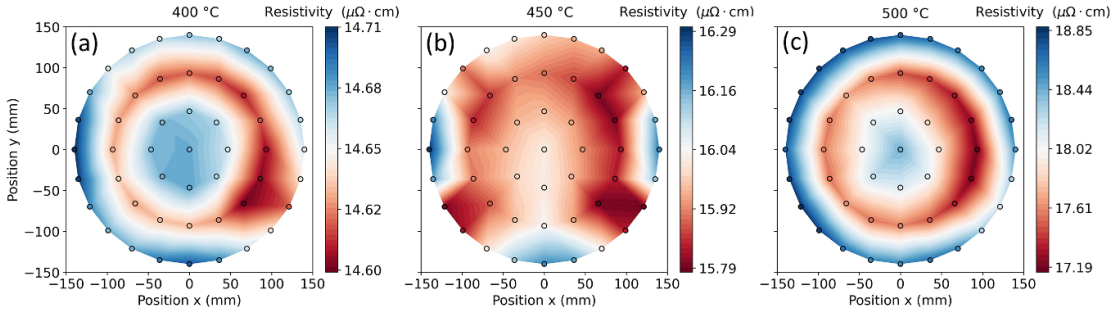

Figure 2. Resistivity maps of the 400 °C (a), 450 °C (b) and 500 °C (c) α-Ta films used for resonator fabrication.

applied to Nb lumped element resonators (60 s in 5.5% HF) that were reported by Verjauw *et al* [36] since it has proven effective to completely remove SiO_x, passivate the Si surface, as well as remove surface niobium oxides, resulting in a Q_i increase by a factor of seven. In total, six different α-Ta chips (three reference chips and three HF-treated chips) were fabricated using the 400 °C, 450 °C and 500 °C α-Ta films. In both reference and HF-treated resonators, the observed Q_i power dependence (figure 3(a)) indicates the presence of dominating TLS depolarization in our devices which is suppressed (saturated) at high photon powers [57]. In the high photon number regime ($Q_{i,high}$) the reference and HF-treated resonators measured (figure 3(b)) exhibit $Q_{i,high}$ values up to $55{\cdot}10^6$. As expected, the HF-treated resonators did not show much difference compared to the reference resonators in this high-power regime, in line with the hypothesis that surface related TLS losses are suppressed (saturated) in this regime and reducing the TLS density therefore has negligible effect. The behavior is different for low power $Q_{i's}$ ($Q_{i,low}$), where no such saturation of loss takes place. The measured reference resonators have values ranging from $0.3{\cdot}10^6$ to $1.2{\cdot}10^6$. After the HF treatment, the $Q_{i,low}$ values increase (figure 3(c)) and vary between $0.2{\cdot}10^6$ and $4.5{\cdot}10^6$. The larger spread observed in the $Q_{i,high}$ and $Q_{i,low}$ of the resonators patterned in the 500 °C HF-treated α-Ta films compared to the 400 °C and 450 °C HF-treated α-Ta films comes from three resonators that show little Q_i dependence as a function of photon number (see supplemental figure S3), indicating that other dissipation mechanisms different from TLS dissipation, such as trapped vortices [58], dominate resonator loss. Besides the spread in the Q_i values, the three types of α-Ta films do not show a significant $Q_{i,high}$ and $Q_{i,low}$ difference. Differences in $Q_{i,low}$ could have been anticipated based on the XRD and resistivity data due to the differences in grain boundary densities of the three α-Ta films since grain boundary dissipation has been identified as a relevant relaxation mechanisms in nominal identical qubits fabricated in different types of Nb films [16]. The fact that $Q_{i,low}$ does not scale with grain boundary density in our study can be explained by the fact that differences are too small or that loss from grain boundaries is not as relevant in α-Ta films as it is in Nb films.

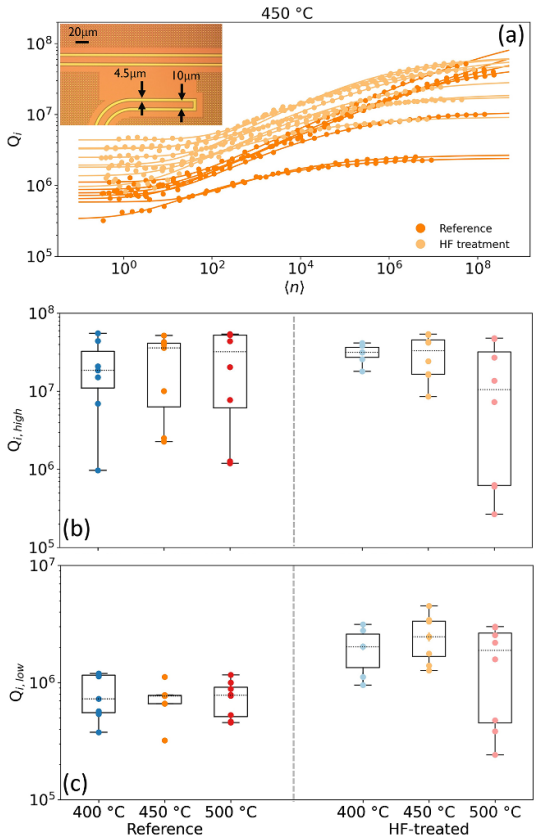

Figure 3. (a) Internal quality factor (Q_i) as a function of estimated mean photon number for reference and HF-treated resonators. Lines are fittings to equation (1). (b) and (c) Boxplot summary of $Q_{i,\,high}$ and $Q_{i,\,low}$ of the reference and HF-treated Ta resonators.

4. Resonator interface characterization

To investigate the increase in $Q_{i,low}$ after the surface treatment, we next study the morphology and composition of the M-A, M-S and S-A interfaces, regions that typically host dominant loss sources [59]. We conduct a detailed characterization of both reference (figure 4) and HF-treated (figure 5) resonators using scanning transmission electron microscopy (STEM) and energy-dispersive x-ray spectroscopy (EDS). All STEM images were taken no longer than 12 h after the HF treatment to mimic the conditions under which resonator Q-factors are measured. In the reference resonators, the top M-A interface (figure 4(b)) is covered by a 3.7 nm tantalum oxide layer, while the tantalum oxide at the side wall is about 6 nm thick. This difference arises from the oxygen plasma treatments [60] during the resonator fabrication and resonator cleaning processes. After the metal etch an oxygen plasma step is first applied to clean post etch residues. During this step the top metal surface is protected by a SiO_2 hard mask, while the side walls are exposed to the plasma. Subsequently, the second oxygen plasma treatment is applied to clean individual chips once the protective resist for dicing has been removed. Since no SiO_2 hard mask is present this time, oxide can grow on every surface. The S-A interface (figures 4(c) and (d)) contains approximately 3 nm thick SiO_x and forms during the fabrication process, although the native SiO_x was initially removed with the HF clean prior to Ta deposition. The M-S interface (figures 4(e) and (f)) is approximately 4 nm thick and consists of a mixture of Si and Ta, as shown by the contrast change in the high-angle annular dark-field-STEM image of the same region (figure 4(f)). This intermixing occurs due to the short-range diffusion of Si into Ta sputtered layers at elevated temperature [61, 62]. No oxygen can be detected above the background value in the M-S interface from the EDS map (figure 4(g)). The absence of a marked O signal across the Si-Ta interface implies negligible oxide growth in the time between the substrate HF clean and the metal deposition. Similar results are obtained also for 450 °C and 500 °C patterned Ta films (see supplementary figures S1 and S2 for STEM images of the resonators patterned using 450 °C and 500 °C α-Ta films). For the HF-treated resonators, the tantalum oxide thickness at the M-A interface (figure 5(b)) is reduced by 1.2–1.5 nm, while SiO_x is completely removed on the S-A interface. The M-S interface is not exposed to the HF post-processing clean and is therefore not affected. The reduction of surface oxides at both the M-A and S-A interfaces likely explains the observed increase in $Q_{i,low}$, as these oxides constitute significant sources of TLS.

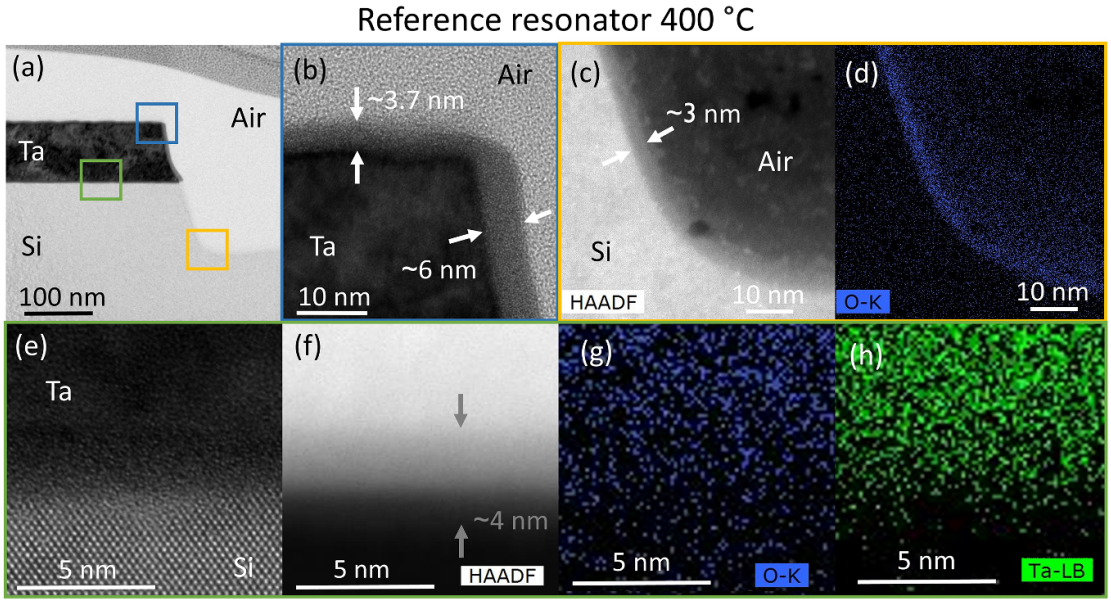

Figure 4. STEM and EDS images of a 400 °C reference α-Ta resonator cross section. (a) Low magnification STEM cross section of Ta resonator. The colored squares mark the areas where high magnification images were taken. (b) STEM cross section of the M-A interface. Arrows indicate the tantalum oxide layer. (c) HAADF-STEM image of the S-A interface. The arrows indicate the silicon oxide layer present. (d) Oxygen EDS map of the S-A interface. (e) STEM image of the S-M interface. (f) HAADF-STEM image of the S-M interface. The arrows indicate the extension of the Si-Ta interfacial layer. (g) Oxygen EDS map of the S-A interface. (h) Tantalum EDS map of the S-A interface.

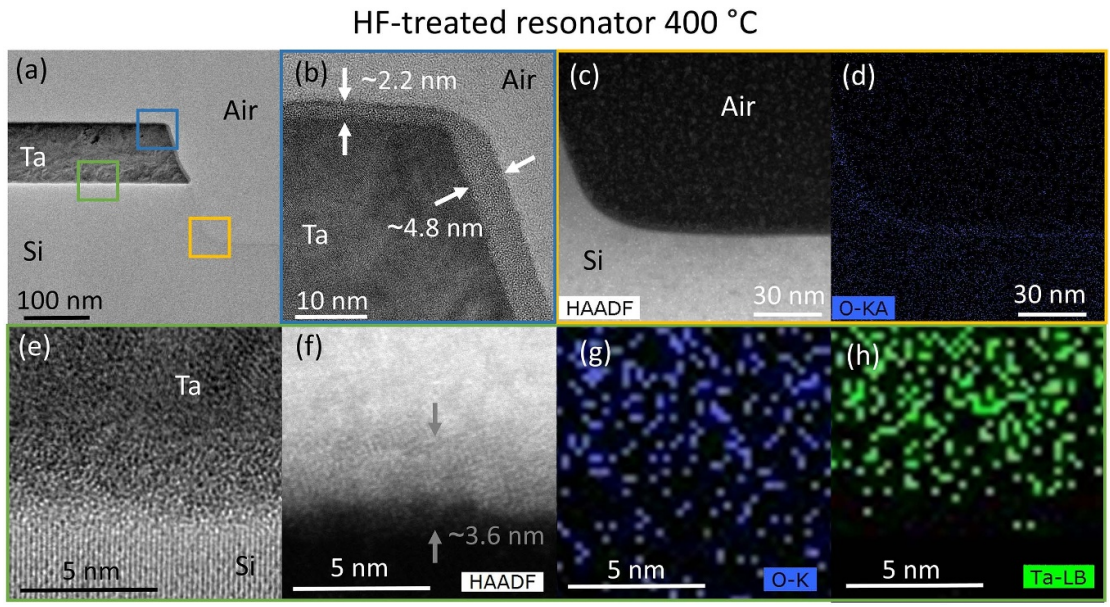

Figure 5. STEM and EDS images of a 400 °C HF-treated α-Ta resonator cross section. (a) Low magnification STEM cross section of Ta resonator. The coloured squares mark the areas where high magnification images were taken. (b) STEM cross section of the M-A interface. Arrows indicate the tantalum oxide layer. (c) HAADF-STEM image of the S-A interface. (d) Oxygen EDS map of the S-A interface. (e) STEM image of the S-M interface. (f) HAADF-STEM image of the S-M interface. The arrows indicate the extension of the Si-Ta interfacial layer. (g) Oxygen EDS map of the S-A interface. (h) Tantalum EDS map of the S-A interface.

Finally, x-ray photoelectron spectroscopy (XPS) is used to investigate the chemical composition of the M-A interface in both reference and HF-treated resonators. The doublet peaks situated at 21.6 eV (figures 6(a)–(c)) corresponds to metallic Ta, while the doublet peak situated at around 26.3 eV corresponds to tantalum pentoxide (Ta_2O_5). The similarities between these XPS spectra suggest that the film properties difference on texture and resistivity afore mentioned do not influence the tantalum oxide formation. By fitting the XPS signal (figure 6(d)), the atomic concentration of the different compounds at the M-A surface can be extracted. Ta_2O_5 is the main tantalum oxide detected, although a small percentage of tantalum

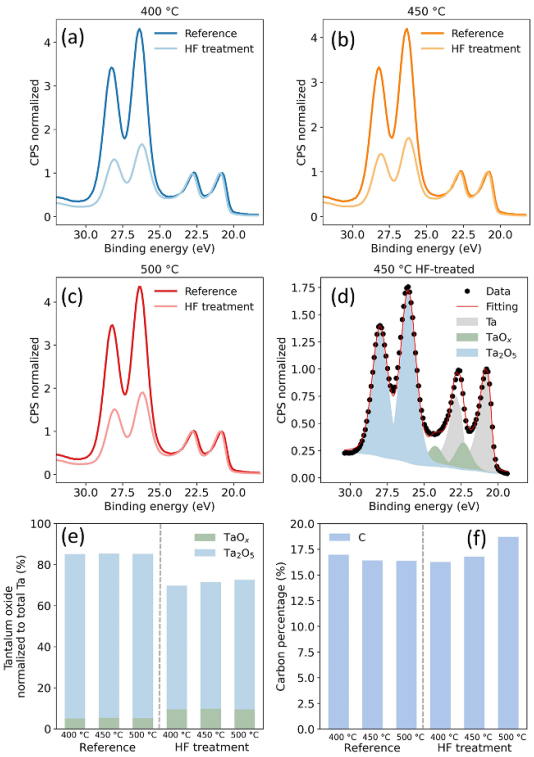

Figure 6. (a)–(c) XPS spectra of a reference and HF-treated Ta chips fabricated using the 400 °C, 450 °C and 500 °C Ta films. (d) Fitting of the XPS spectra of a HF-treated chip fabricated using the 450 °C Ta film. Black dots are experimental data, red line is the fitting. The blue area represents the contribution to the fitting Ta_2O_5, the grey area corresponds to the contribution of metallic Ta, and the green area the contribution from TaO_x. (e) Ta_2O_5 and TaO_x percentage respect to the total amount of Ta detected in the reference and HF-treated resonators. (f) Percentage of C detected in the reference and HF-treated resonators.

suboxide (TaO_x) is also identified. The proportion of Ta_2O_5 and TaO_x detected is similar in the 400 °C, 450 °C and 500 °C reference resonators. This is expected since the thickness of the top tantalum oxide layer in the three different films is comparable, as shown in the STEM images. After the HF treatment the total amount of tantalum oxides detected decreases between 15%–18%. This reduction is mostly due to the removal of Ta_2O_5 (figure 6(e)) since the amount of TaO_x increases after the HF-treatment. These observations align with the measurements and modeling of tantalum oxide profiles presented by McLellan *et al* [63] where Ta_2O_5, the oxide closest to the surface, is the first to be removed during chemical treatment. Carbon peaks are also observed in the XPS spectra of the patterned M-A interface, which are also fitted to extract the C atomic concentration. The carbon (C) content is similar in all samples (figure 6(f)), except in the 500 °C HF-treated sample, where it is around 2% higher than the other films. This suggests that hydrocarbon residues might penetrate through grain boundaries deeper than 1 nm into the surface, since it is approximately the Ta_2O_5 thickness removed by the HF treatment.

5. Resonator modeling

To isolate material-specific TLS defect microwave loss we analyze Q_i as a function of $\langle n \rangle$ using the following standard model [53]:

$$\frac{1}{Q_i} = F tan(\delta_0) \frac{tanh\left(\frac{hf_r}{2k_BT}\right)}{\left(1+\left(\frac{<n>}{n_c}\right)\right)^b} + \delta_{other} \tag{1}$$

where F is the participation ratio, $\tan\delta_0$ is the intrinsic loss tangent for the material containing the TLS and δ_{other} is the contribution from power independent non-TLS loss. Similarly, n_c is the critical photon number equivalent to the saturation field of different TLSs and b is a phenomenological parameter, which is 0.5 for noninteracting TLS defects [64] and lower than 0.5 in the presence of TLS-TLS interactions [65]. Furthermore, h is the Planc constant, f_r is resonator frequency, k_B is Boltzmann constant and T is the temperature. Since measurements were performed at the base temperature of the dilution refrigerator

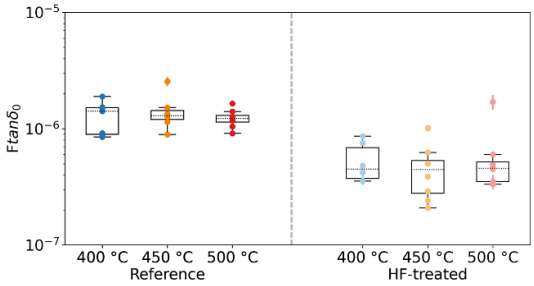

Figure 7. Boxplot of the $F\tan\delta_0$ extracted from fitting the reference and HF-treated Ta resonators resonator data to equation (1). The boxes extend from the first quartile to the third quartile of $F\tan\delta_0$ with a line at the median. The whiskers extend from the box by 1.5 times the inter-quartile range.

($T = 10$ mK), tanh factor is close to 1. Our data agrees well with the above model across all measured resonators (figure 4(a) and supplementary figures S3(a)–(c)). The extracted TLS loss, as expressed by $F\tan\delta_0$ (figure 7), is similar for the reference resonators in the three different α-Ta films with values ranging from $0.8{\cdot}10^{-6}$–$1.9{\cdot}10^{-6}$. For the HF-treated samples, $F\tan\delta_0$ decreases displaying values within the range of $0.2{\cdot}10^{-6}$–$1.7{\cdot}10^{-6}$, with median values decreasing by a factor of three when compared to the reference resonators. Like the previous analysis, there are no significant differences in $F\tan\delta_0$ among the three types of films utilized. This suggests that intrinsic film properties such as texture and resistivity do not currently limit the TLS loss. Regarding other fitting parameters, the b parameter is generally less than 0.5 (supplementary figure S4(b)), which aggress with previously b values reported [36] in resonators with Q_i around and above $1{\cdot}10^6$, indicating that TLS-TLS interactions are present. Critical photon numbers in α-Ta devices are found to be $n_c = 1-50$, except for the HF-treated resonators fabricated with 400 °C α-Ta where n_c can reach up to 150 photons (supplemental figure S4(c)).

6. Discussion

The observed reduction in TLS loss can be attributed primarily to a decrease in surface oxides, both at the M-A interface and the S-A interface. This reduction is evident in both the STEM images (figures 4(c) and (d), figures 5(c) and (d)) and the XPS analysis (figure 6(e)), where the amount of surface tantalum oxide decreases following the HF treatment, while the SiO_x is completely removed, and no reoxidation is observed in the time before the measurement. Determining the impact of removing Ta_2O_5 on reducing TLS loss is challenging due to the concurrent increase in the amount of TaO_x. It could happen that the dielectric loss of TaO_x is greater than that of Ta_2O_5. As a result, a significant reduction in Ta_2O_5-related TLS loss may be offset by a slight increase in TaO_x. In addition, the fact the carbon content in the reference and HF-treated resonators is similar indicates that the TLS loss contribution from hydrocarbon residues has to be smaller than the median TLS loss of approximately $0.45{\cdot}10^{-6}$ in HF-treated samples which encompasses the TLS loss contribution from all interfaces and the substrate. These observations suggest that although the total dielectric loss in CPW resonators has different sources, surface oxides are still the main contribution in non-treated samples.

On average, the $Q_{i,low}$ values after the HF treatment obtained in this work are around $2{\cdot}10^6$. These values are in the range of α-Ta CPW resonators of similar size reported on both Si [46] and sapphire [44, 48]. Transmon qubits made of α-Ta with record Q_i of $7.1{\cdot}10^6$ and $11.8{\cdot}10^6$ have also been reported by Place *et al* [32] and Wang *et al* [33], respectively, while our record $Q_{i,low}$ is $4.5{\cdot}10^6$. However, due to differences in device geometry a direct quality factor comparison between qubits and resonators is difficult because of differences in the energy participation ratio of the interfaces. Another possibility for the quality factor difference is loss added by the M-S interface. In our samples no oxide is detected at the M-S interface (figure 4(h)), but there is evidence of Si diffusion into the Ta film (figures 4(e) and (f)), while in the α-Ta qubit samples reported in literature the M-S interface shows an atomically sharp boundary between Ta and sapphire [32]. Different tantalum silicide compounds are known to form at the Ta-Si interface when exposed to elevated temperatures. The formation of pentatantalum trisilicide (Ta_5Si_3) occurs when Ta films deposited on Si substrates are annealed at 550 °C–600 °C for one hour [66], while tantalum silicide ($TaSi_2$) requires temperatures around 785 °C [67]. These silicides are metallic [68, 69] and their presence at the M-S interface of superconducting devices might affect device performance. It is unlikely that these silicides are present at the M-S interface of our Ta resonator chips, since the maximum temperature used in the growth of these films is 500 °C, and all depositions were completed in less than ten minutes. As demonstrated by Cheng [62],

the Ta-Si interfacial layer thickness can be controlled by modifying the annealing temperature or the annealing time. However, our STEM images indicate that the deposition temperature has no effect on the interfacial layer thickness (supplemental figures S1 and S2). Further investigations on the effect of the deposition time at elevated temperatures will be needed to conclude if the Ta-Si interfacial layer can be controlled and if this layer negatively affects device performance.

7. Conclusion

This study demonstrates the fabrication of superconducting high-quality α-Ta coplanar-waveguide resonators directly grown on pristine Si over a large temperature processing window. The combination of spectroscopy and microscopy enables us to investigate the composition and structure of the different resonator interfaces and to establish correlations with device loss. Our analysis shows that the removal of surface oxides leads to factor of three reduction of median TLS loss, while intrinsic film properties such as crystallinity and resistivity do not seem to play any role at the current loss level. Our work opens the possibility for integrating α-Ta as a low-loss material in the fabrication of larger and more complex superconducting devices, as well as making it compatible with fabrication in industrial-grade facilities. In addition, simulations [70, 71] of studied structures incorporating the material insight gained and the superconducting nature of the systems could contribute to the better understanding of the devices. The potential of this multidisciplinary approach to understand the material origin of loss sources paves the way to engineer high performance superconducting devices, as well as other quantum or classical technologies that benefit from low-loss superconducting materials such as trapped ions [72] microwave kinetic inductance detectors [73] single photon detectors [74, 75] and superconducting filters [76].

Data availability statements

The data that support the findings of this study are openly available at the following URL/DOI: http://doi.org/10.5281/zenodo.10447511.

Acknowledgments

The authors gratefully thank Paola Favia, Olivier Richard, Chris Drijbooms, Ilse Hoflijk, Thierry Conard, Céline Noël, Valentina Spampinato, Alexis Franquet for metrology support. This work was supported in part by the imec Industrial Affiliation Program on Quantum Computing. We also thanks Nathalie de Leon for useful discussions and comments about this work.

Funding

This project leading to this application has received funding from the ECSEL Joint Undertaking (JU) under Grant Agreement No. 101007322. The JU receives support from the European Union's Horizon 2020 research and innovation program and Germany, France, Belgium, Austria, Netherlands, Finland, Israel. (Please visit the project website www.matqu.eu for more information). This work was supported by imec's Industrial Affiliation Program on Quantum Computing.

ORCID iDs

D P Lozano https://orcid.org/0000-0003-3098-3266
J Van de Vondel https://orcid.org/0000-0001-6894-7258
A Potočnik https://orcid.org/0000-0002-0352-6388

References

[1] Devoret M H and Schoelkopf R J 2013 Superconducting circuits for quantum information: an outlook *Science* **339** 1169
[2] You J Q and Nori F 2005 Superconducting circuits and quantum information *Phys. Today* **58** 42
[3] Wang C, Axline C, Gao Y Y, Brecht T, Chu Y, Frunzio L, Devoret M H and Schoelkopf R J 2015 Surface participation and dielectric loss in superconducting qubits *Appl. Phys. Lett.* **107** 162601
[4] Werninghaus M, Egger D J, Roy F, Machnes S, Wilhelm F K and Filipp S 2021 Leakage reduction in fast superconducting qubit gates via optimal control *npj Quantum Inf.* **7** 14
[5] Kelly J *et al* 2014 Optimal quantum control using randomized benchmarking *Phys. Rev. Lett.* **112** 240504
[6] Kreikebaum J M, Dove A, Livingston W, Kim E and Siddiqi I 2016 Optimization of infrared and magnetic shielding of superconducting TiN and Al coplanar microwave resonators *Supercond. Sci. Technol.* **29** 104002

[7] Wang Z, Shankar S, Minev Z K, Campagne-Ibarcq P, Narla A and Devoret M H 2019 Cavity attenuators for superconducting qubits *Phys. Rev. Appl.* **11** 014031
[8] Siddiqi I 2021 Engineering high-coherence superconducting qubits *Nat. Rev. Mater.* **6** 875
[9] de Leon N P, Itoh K M, Kim D, Mehta K K, Northup T E, Paik H, Palmer B S, Samarth N, Sangtawesin S and Steuerman D W 2021 Materials challenges and opportunities for quantum computing hardware *Science* **372** eabb2823
[10] Lee D, DuBois J L and Lordi V 2014 Identification of the local sources of paramagnetic noise in superconducting qubit devices fabricated on α-Al_2O_3 substrates using density-functional calculations *Phys. Rev. Lett.* **112** 017001
[11] Un S, de Graaf S, Bertet P, Kubatkin S and Danilov A 2022 On the nature of decoherence in quantum circuits: revealing the structural motif of the surface radicals in α-Al_2O_3 *Sci. Adv.* **8** eabm6169
[12] de Graaf S E, Adamyan A A, Lindström T, Erts D, Kubatkin S E, Tzalenchuk A Y and Danilov A V 2017 Direct identification of dilute surface spins on Al_2O_3: origin of flux noise in quantum circuits *Phys. Rev. Lett.* **118** 057703
[13] Fritz S, Seiler A, Radtke L, Schneider R, Weides M, Weiß G and Gerthsen D 2018 Correlating the nanostructure of Al-Oxide with deposition conditions and dielectric contributions of two-level systems in perspective of superconducting quantum circuits *Sci. Rep.* **8** 7956
[14] Megrant A *et al* 2012 Planar superconducting resonators with internal quality factors above one million *Appl. Phys. Lett.* **100** 113510
[15] Richardson C J K, Siwak N P, Hackley J, Keane Z K, Robinson J E, Arey B, Arslan I and Palmer B S 2016 Fabrication artifacts and parallel loss channels in metamorphic epitaxial aluminum superconducting resonators *Supercond. Sci. Technol.* **29** 064003
[16] Premkumar A *et al* 2021 Microscopic relaxation channels in materials for superconducting qubits *Commun. Mater.* **2** 72
[17] Sendelbach S, Hover D, Kittel A, Mück M, Martinis J M and McDermott R 2008 Magnetism in SQUIDs at millikelvin temperatures *Phys. Rev. Lett.* **100** 227006
[18] Kumar P, Sendelbach S, Beck M A, Freeland J W, Wang Z, Wang H, Yu C C, Wu R Q, Pappas D P and McDermott R 2016 Origin and reduction of 1/*f* magnetic flux noise in superconducting devices *Phys. Rev. Appl.* **6** 041001
[19] Murthy A A, Lee J, Kopas C, Reagor M J, McFadden A P, Pappas D P, Checchin M, Grassellino A and Romanenko A 2022 TOF-SIMS analysis of decoherence sources in superconducting qubits *Appl. Phys. Lett.* **120** 044002
[20] Altoé M V P *et al* 2022 Localization and mitigation of loss in niobium superconducting circuits *PRX Quantum* **3** 020312
[21] Vissers M R, Gao J, Wisbey D S, Hite D A, Tsuei C C, Corcoles A D, Steffen M and Pappas D P 2010 Low loss superconducting titanium nitride coplanar waveguide resonators *Appl. Phys. Lett.* **97** 232509
[22] Ohya S *et al* 2013 Room temperature deposition of sputtered TiN films for superconducting coplanar waveguide resonators *Supercond. Sci. Technol.* **27** 015009
[23] Kim S, Terai H, Yamashita T, Qiu W, Fuse T, Yoshihara F, Ashhab S, Inomata K and Semba K 2021 Enhanced coherence of all-nitride superconducting qubits epitaxially grown on silicon substrate *Commun. Mater.* **2** 98
[24] Yu C X, Zihlmann S, Troncoso Fernández-Bada G, Thomassin J-L, Gustavo F, Dumur É and Maurand R 2021 Magnetic field resilient high kinetic inductance superconducting niobium nitride coplanar waveguide resonators *Appl. Phys. Lett.* **118** 054001
[25] Bruno A, de Lange G, Asaad S, van der Enden K L, Langford N K and DiCarlo L 2015 Reducing intrinsic loss in superconducting resonators by surface treatment and deep etching of silicon substrates *Appl. Phys. Lett.* **106** 182601
[26] Müller M *et al* 2022 Magnetic field robust high quality factor NbTiN superconducting microwave resonators *Mater. Quantum Technol.* **2** 015002
[27] Samkharadze N, Bruno A, Scarlino P, Zheng G, DiVincenzo D P, DiCarlo L and Vandersypen L M K 2016 High-kinetic-inductance superconducting nanowire resonators for circuit QED in a magnetic field *Phys. Rev. Appl.* **5** 044004
[28] Grünhaupt L *et al* 2019 Granular aluminium as a superconducting material for high-impedance quantum circuits *Nat. Mater.* **18** 816
[29] Winkel P, Borisov K, Grünhaupt L, Rieger D, Spiecker M, Valenti F, Ustinov A V, Wernsdorfer W and Pop I M 2020 Implementation of a transmon qubit using superconducting granular aluminum *Phys. Rev.* X **10** 031032
[30] Song C, Heitmann T W, DeFeo M P, Yu K, McDermott R, Neeley M, Martinis J M and Plourde B L T 2009 Microwave response of vortices in superconducting thin films of Re and Al *Phys. Rev.* B **79** 174512
[31] McRae C R H, Béjanin J H, Earnest C T, McConkey T G, Rinehart J R, Deimert C, Thomas J P, Wasilewski Z R and Mariantoni M 2018 Thin film metrology and microwave loss characterization of indium and aluminum/indium superconducting planar resonators *J. Appl. Phys.* **123** 205304
[32] Place A P M *et al* 2021 New material platform for superconducting transmon qubits with coherence times exceeding 0.3 milliseconds *Nat. Commun.* **12** 1779
[33] Wang C *et al* 2022 Towards practical quantum computers: transmon qubit with a lifetime approaching 0.5 milliseconds *npj Quantum Inf.* **8** 3
[34] Face D W, Prober D E, McGrath W R and Richards P L 1986 High quality tantalum superconducting tunnel junctions for microwave mixing in the quantum limit *Appl. Phys. Lett.* **48** 1098
[35] Gaidis M C 1994 Superconducting tunnel junctions as single photon x-ray detectors *PhD Thesis* Yale University (available at: https://orbis.library.yale.edu/vwebv/holdingsInfo?searchId=457&recCount=50&recPointer=3&bibId=4475583)
[36] Verjauw J *et al* 2021 Investigation of microwave loss induced by oxide regrowth in high-Q niobium resonators *Phys. Rev. Appl.* **16** 014018
[37] Braginsky V B, Ilchenko V S and Bagdassarov K S 1987 Experimental observation of fundamental microwave absorption in high-quality dielectric crystals *Phys. Lett.* A **120** 300
[38] Luiten A N, Mann A G and Blair D G 1993 Ultrahigh Q-factor cryogenic sapphire resonator *Electron. Lett.* **29** 879
[39] Krupka J, Derzakowski K, Abramowicz A, Tobar M E and Geyer R G 1999 Use of whispering-gallery modes for complex permittivity determinations of ultra-low-loss dielectric materials *IEEE Trans. Microw. Theory Tech.* **47** 752
[40] Melville A *et al* 2020 Comparison of dielectric loss in titanium nitride and aluminum superconducting resonators *Appl. Phys. Lett.* **117** 124004
[41] Gambetta J M, Murray C E, Fung Y-K-K, McClure D T, Dial O, Shanks W, Sleight J W and Steffen M 2017 Investigating surface loss effects in superconducting transmon qubits *IEEE Trans. Appl. Supercond.* **27** 1–5
[42] Gaidis M C, Friedrich S, Prober D E, Szymkowiak A E and Moseley S H 1993 Superconducting Nb–Ta–Al–AlO_x–Al tunnel junctions for x-ray detection *J. Low Temp. Phys.* **93** 605
[43] Barends R, Baselmans J J A, Hovenier J N, Gao J R, Yates S J C, Klapwijk T M and Hoevers H F C 2007 Niobium and tantalum high Q resonators for photon detectors *IEEE Trans. Appl. Supercond.* **17** 263
[44] Alegria L D, Tennant D M, Chaves K R, Lee J R I, O'Kelley S R, Rosen Y J and DuBois J L 2023 Two-level systems in nucleated and non-nucleated epitaxial alpha-tantalum films *Appl. Phys. Lett.* **123** 062601

[45] Kurter C et al 2022 Quasiparticle tunneling as a probe of Josephson junction barrier and capacitor material in superconducting qubits Npj Quantum Inf. 8 31
[46] Grigoras K et al 2022 Qubit-compatible substrates with superconducting through-silicon vias IEEE Trans. Quantum Eng. 3 1–10
[47] Müller C, Cole J H and Lisenfeld J 2019 Towards understanding two-level-systems in amorphous solids: insights from quantum circuits Rep. Prog. Phys. 82 124501
[48] Shi L et al 2022 Tantalum microwave resonators with ultra-high intrinsic quality factors Appl. Phys. Lett. 121 242601
[49] Gladczuk L, Patel A, Singh Paur C and Sosnowski M 2004 Tantalum films for protective coatings of steel Thin Solid Films 467 150
[50] Abadias G, Colin J J, Tingaud D, Djemia P, Belliard L and Tromas C 2019 Elastic properties of α- and β-tantalum thin films Thin Solid Films 688 137403
[51] Donohue H, Gris H, Yeoh J C and Buchanan K 2002 Low-resistivity PVD α -tantalum: phase formation and integration in ultra-low k dielectric/copper damascene structures Proc. IEEE 2002 Int. Interconnect Technology Conf. (Cat. No.02EX519) pp 179–81
[52] Crowley K D et al 2023 Disentangling losses in tantalum superconducting circuits Phys. Rev. X 13 041005
[53] Bishara H, Lee S, Brink T, Ghidelli M and Dehm G 2021 Understanding grain boundary electrical resistivity in Cu: the effect of boundary structure ACS Nano 15 16607
[54] Wan D et al 2021 Fabrication and room temperature characterization of trilayer junctions for the development of superconducting qubits on 300 mm wafers Jpn. J. Appl. Phys. 60 SBBI04
[55] Probst S, Song F B, Bushev P A, Ustinov A V and Weides M 2015 Efficient and robust analysis of complex scattering data under noise in microwave resonators Rev. Sci. Instrum. 86 024706
[56] Martinis J M and Megrant A 2014 UCSB final report for the CSQ program: review of decoherence and materials physics for superconducting qubits (arXiv:1410.5793)
[57] Burnett J, Bengtsson A, Niepce D and Bylander J 2018 Noise and loss of superconducting aluminium resonators at single photon energies J. Phys.: Conf. Ser. 969 012131
[58] Bothner D, Gaber T, Kemmler M, Koelle D and Kleiner R 2011 Improving the performance of superconducting microwave resonators in magnetic fields Appl. Phys. Lett. 98 102504
[59] Woods W, Calusine G, Melville A, Sevi A, Golden E, Kim D K, Rosenberg D, Yoder J L and Oliver W D 2019 Determining interface dielectric losses in superconducting coplanar-waveguide resonators Phys. Rev. Appl. 12 014012
[60] Zhang Z et al 2019 The mechanism study of mixed Ar/O_2 plasma-cleaning treatment on niobium surface for work function improvement Appl. Surf. Sci. 475 143
[61] Gallais P, Hantzpergue J J, Remy J C and Roptin D 1988 Sputter deposition of thin tantalum layers and low temperature interactions between tantalum and SiO_2 and tantalum and silicon Thin Solid Films 165 227
[62] Cheng J Y and Chen L J 1991 Growth kinetics of amorphous interlayers by solid-state diffusion in ultrahigh vacuum deposited polycrystalline Nb and Ta thin films on (111)Si J. Appl. Phys. 69 2161
[63] McLellan R A et al 2023 Chemical profiles of the oxides on tantalum in state of the art superconducting circuits Adv. Sci. 10 2300921
[64] Phillips W A 1972 Tunneling states in amorphous solids J. Low Temp. Phys. 7 351
[65] de Graaf S E, Faoro L, Burnett J, Adamyan A A, Tzalenchuk A Y, Kubatkin S E, Lindström T and Danilov A V 2018 Suppression of low-frequency charge noise in superconducting resonators by surface spin desorption Nat. Commun. 9 1143
[66] Noya A, Takeyama M, Sasaki K and Nakanishi T 1994 First phase nucleation of metal-rich silicide in Ta/Si systems J. Appl. Phys. 76 3893
[67] Christou A and Day H M 1976 Silicide formation and interdiffusion effects in Si-Ta, SiO_2-Ta AND Si-PtSi-Ta thin film structures J. Electron. Mater. 5 1–12
[68] Murarka S P and Fraser D B 1980 Silicide formation in thin cosputtered (tantalum+silicon) films on polycrystalline silicon and SiO_2 J. Appl. Phys. 51 1593
[69] Ravindra N M, Jin L, Ivanov D, Mehta V R, Dieng L M, Popov G, Gokce O H, Grow J and Fiory A T 2002 Electrical and compositional properties of $TaSi_2$ films J. Electron. Mater. 31 1074
[70] Nagai Y, Shinohara Y, Futamura Y, Ota Y and Sakurai T 2013 Numerical construction of a low-energy effective Hamiltonian in a self-consistent Bogoliubov–de Gennes approach of superconductivity J. Phys. Soc. Japan 82 094701
[71] Pomorski K and Stojewski B 2024 Hybrid Schrödinger-Ginzburg-Landau (Sch-GL) approach to study of superconducting integrated structures Mol. Cryst. Liq. Cryst. 768 101
[72] Hite D A, Colombe Y, Wilson A C, Allcock D T C, Leibfried D, Wineland D J and Pappas D P 2013 Surface science for improved ion traps MRS Bull. 38 826
[73] Ulbricht G, De Lucia M and Baldwin E 2021 Applications for microwave kinetic induction detectors in advanced instrumentation Appl. Sci. 11 2671
[74] Esmaeil Zadeh I, Chang J, Los J W N, Gyger S, Elshaari A W, Steinhauer S, Dorenbos S N and Zwiller V 2021 Superconducting nanowire single-photon detectors: a perspective on evolution, state-of-the-art, future developments, and applications Appl. Phys. Lett. 118 190502
[75] Wolff M A, Vogel S, Splitthoff L and Schuck C 2020 Superconducting nanowire single-photon detectors integrated with tantalum pentoxide waveguides Sci. Rep. 10 17170
[76] Attar S S, Setoodeh S, Laforge P D, Bakri-Kassem M and Mansour R R 2014 Low temperature superconducting tunable bandstop resonator and filter using superconducting RF MEMS varactors IEEE Trans. Appl. Supercond. 24 1